

# Ultrafast photothermoelectric effect in Dirac semimetallic $\text{Cd}_3\text{As}_2$ revealed by terahertz emission

Wei Lu<sup>1,2</sup>, Zipu Fan<sup>2</sup>, Yunkun Yang<sup>3</sup>, Junchao Ma<sup>2</sup>, Jiawei Lai<sup>2</sup>, Xiaoming Song<sup>1</sup>, Xiao Zhuo<sup>2</sup>, Zhaoran Xu<sup>2</sup>, Jing Liu<sup>1</sup>, Xiaodong Hu<sup>1</sup>, Shuyun Zhou<sup>4,5</sup>, Faxian Xiu<sup>3</sup>, Jinluo Cheng<sup>6</sup> & Dong Sun<sup>2,5</sup>✉

The thermoelectric effects of topological semimetals have attracted tremendous research interest because many topological semimetals are excellent thermoelectric materials and thermoelectricity serves as one of their most important potential applications. In this work, we reveal the transient photothermoelectric response of Dirac semimetallic  $\text{Cd}_3\text{As}_2$ , namely the photo-Seebeck effect and photo-Nernst effect, by studying the terahertz (THz) emission from the transient photocurrent induced by these effects. Our excitation polarization and power dependence confirm that the observed THz emission is due to photothermoelectric effect instead of other nonlinear optical effect. Furthermore, when a weak magnetic field ( $\sim 0.4$  T) is applied, the response clearly indicates an order of magnitude enhancement on transient photothermoelectric current generation compared to the photo-Seebeck effect. Such enhancement supports an ambipolar transport nature of the photo-Nernst current generation in  $\text{Cd}_3\text{As}_2$ . These results highlight the enhancement of thermoelectric performance can be achieved in topological Dirac semimetals based on the Nernst effect, and our transient studies pave the way for thermoelectric devices applicable for high field circumstance when nonequilibrium state matters. The large THz emission due to highly efficient photothermoelectric conversion is comparable to conventional semiconductors through optical rectification and photo-Dember effect.

<sup>1</sup>State Key Laboratory of Precision Measurement Technology and Instruments, School of Precision Instruments and Opto-electronics Engineering, Tianjin University, Tianjin 300072, China. <sup>2</sup>International Center for Quantum Materials, School of Physics, Peking University, Beijing 100871, China. <sup>3</sup>State Key Laboratory of Surface Physics and Department of Physics, Fudan University, Shanghai 200433, China. <sup>4</sup>State Key Laboratory of Low Dimensional Quantum Physics and Department of Physics, Tsinghua University, Beijing 100084, China. <sup>5</sup>Collaborative Innovation Center of Quantum Matter, Beijing 100871, China. <sup>6</sup>Changchun Institute of Optics, Fine Mechanics and Physics, Chinese Academy of Sciences, Changchun 130033, China. ✉email: [sundong@pku.edu.cn](mailto:sundong@pku.edu.cn)

**T**hermoelectric (TE) properties, which determine heat-to-electricity energy conversion of materials, lie at the center toward TE applications. Traditionally, semimetals are usually regarded as bad TE materials, because they naturally possess two types of carriers, which counterbalance each other's contribution to the induced TE voltage, leading to a reduced thermopower compare to semiconductors which usually has unipolar transports<sup>1</sup>. Interestingly, recent TE transport measurements on Weyl semimetals have shown that both types of carriers can contribute to the transverse TE voltage constructively through Nernst effect when a magnetic field is applied perpendicular to the applied temperature gradient, because electrons and holes are forced to deflect in opposite directions by the magnetic force<sup>2–7</sup>. Taking advantage of Nernst effect, four times higher thermopower factor compared to conventional Seebeck response is achieved on NbP<sup>4</sup>, which is comparable to that of the state-of-the-art thermoelectric materials (see Supplementary Table 1 for a summary of thermoelectric coefficients of typical materials).

Different from steady-state TE response, which is usually slow because it involves the heat transport dynamics of lattice, the photothermoelectric (PTE) response upon photoexcitation can be ultrafast as it is dominated by the transient carrier temperature, which is induced by the highly nonequilibrium carriers excited by ultrafast laser pulses<sup>8–12</sup>. The instantaneous transient states after the photoexcitation can support transient ambipolar transport and provide ambipolar TE effect. As such response is usually on the picosecond timescale in semimetals<sup>9,12–14</sup>, such transient current is difficult to be measured by conventional transport measurement. Instead, the picosecond transient current emits electromagnetic wave in terahertz (THz) frequency range, thus can be characterized by measuring its THz emission<sup>15–17</sup>.

The ultrafast PTE response is an important aspect of photo-excited carrier dynamics, which is crucial for high field/speed electronic device applications. With ultrahigh electron mobility and ultrafast carrier dynamics, topological semimetals are suitable for such applications<sup>11,13,18,19</sup>. In these devices, the carriers are accelerated by the electric field which is similar to the photo-excited state after photoexcitation<sup>9,14,20–24</sup>. It is equally important for optoelectronic-related applications, such as light-harvesting and detection, where light interaction with materials is involved and the simultaneous transient optical process involves the TE response of the materials<sup>8,10,11,25–27</sup>.

In this work, we reveal the transient ambipolar TE current response of typical Dirac semimetal Cd<sub>3</sub>As<sub>2</sub> after ultrafast photoexcitation under magnetic field. The transient thermal gradient is created by the thickness gradient of the as-grown Cd<sub>3</sub>As<sub>2</sub> sample after ultrafast photoexcitation. As a contactless approach, the THz emission from the transient TE current is studied at room temperature. Our results clearly distinguish the transverse Seebeck response and the Nernst response from Cd<sub>3</sub>As<sub>2</sub> after photoexcitation. According to the THz emission amplitudes, the Nernst effect is one order of magnitude larger than the Seebeck effect with a relatively weak magnetic field  $B \sim 0.4$  T, and the large enhancement is attributed to the constructive ambipolar transport nature under magnetic field. Furthermore, the efficiency of THz emission from Cd<sub>3</sub>As<sub>2</sub> is comparable to that of typical semiconductor THz sources. This work may open opportunities for high-speed TE devices, taking advantage of their PTE effects.

## Results

### THz emissions from a Cd<sub>3</sub>As<sub>2</sub> film with a thickness gradient.

The Cd<sub>3</sub>As<sub>2</sub> samples measured in this work are [112]-oriented thin films grown by molecular beam epitaxy<sup>28–30</sup>. As shown in our previous study<sup>28</sup>, the Fermi level of Cd<sub>3</sub>As<sub>2</sub> is about 250 meV above the Dirac node, the electron doping density is on the order

of  $10^{13}$  cm<sup>-2</sup>, and the mobility is about  $5 \times 10^3$  cm<sup>2</sup> V<sup>-1</sup> s<sup>-1</sup> at room temperature. The Cd<sub>3</sub>As<sub>2</sub> film has a radial thickness gradient due to the nature of the growth method. The central area is thicker, and the thickness gradually decreases from the center to the outer part on a circular substrate. The gradient is characterized by relative transmittance scanning with a 633-nm He-Ne laser. Figure 1a shows the thickness variation of a Cd<sub>3</sub>As<sub>2</sub> sample deduced from the transmittance measurement. The maximum thickness of the Cd<sub>3</sub>As<sub>2</sub> film is estimated to be around 50 nm. The relative thickness gradient is about 10% per millimeter.

Because the Cd<sub>3</sub>As<sub>2</sub> has strong light absorption at the 800-nm excitation wavelength ( $\sim 50\%$  for 50-nm thick film<sup>31</sup>), the light intensity decays quickly when penetrating into Cd<sub>3</sub>As<sub>2</sub>, which builds up transient temperature gradient of absorbed light energy and thus the electron temperature gradient along the direction perpendicular to the surface. On the other hand, as a result of the radial thickness gradient of Cd<sub>3</sub>As<sub>2</sub> film, the ultrafast pulse excitation can also produce a temperature gradient along the in-plane direction. This effect has been previously experimentally verified in Bi<sub>2</sub>Te<sub>3</sub>-based TE thin films<sup>16</sup>. The temperature gradient, along both out-of-plane and in-plane directions, can generate an out-of-plane ( $J_{\perp}$ ) and in-plane ( $J_{\parallel}$ ) TE current through Seebeck effect, respectively. In our previous studies<sup>11,28</sup>, we have already demonstrated a PTE current in picosecond timescale generated in Cd<sub>3</sub>As<sub>2</sub> when excited by ultrafast pulses. The picosecond currents emit electromagnetic waves in THz frequency, which can be detected in the electro-optical (E-O) sampling geometry.

The measurement of THz emission from ultrafast laser excitation of Cd<sub>3</sub>As<sub>2</sub> is schematically depicted in Fig. 1b, which is based on a typical E-O sampling using [110] orientated ZnTe crystal. In a default experimental configuration at room temperature, an 800-nm 150-femtosecond laser beam excites Cd<sub>3</sub>As<sub>2</sub> film under normal incidence with a magnetic field (when applicable) applied along the  $x$ -axis, and the E-O sampling is configured to detect  $y$ -polarized THz signal (with ZnTe[110] along  $x$ -axis). More experimental details of transient THz emission setup can be found in the method section and the detail of THz sampling geometry can be found in Supplementary Note 2.

As shown in Fig. 1c, the THz field emitted by the in-plane TE current ( $J_{\parallel}$ ) is determined by the following relation:  $E_{\parallel}(t) \propto dJ_{\parallel}/dt$ , which propagates along the light path ( $z$ -axis). The THz field emitted by the out-of-plane TE current  $J_{\perp}$  cannot be detected in the E-O sampling geometry. However, when the sample is tilted,  $J_{\perp}$  would have projection perpendicular to  $z$ -axis, which contributes to detectable THz emission (see Supplementary Note 3). Alternatively, when an  $x$ -direction magnetic field is applied, a  $y$ -direction current  $J_N$  is generated from Nernst effect as determined later on. Both approaches can emit detectable THz in the aforementioned E-O sampling geometry.

Figure 1d shows typical THz emission signals detected in E-O sampling with and without magnetic field. According to the magnitudes of THz emission signals ( $S(J_{\parallel})$  and  $S(J_{\perp})$ ) emitted from  $J_{\parallel}$  and  $J_{\perp}$ , respectively, we can find that  $J_{\perp}$  is stronger than  $J_{\parallel}$  when no magnetic field is applied. Furthermore, when an  $x$ -direction magnetic field of  $B = 0.4$  T is applied, the THz emission signal ( $S(J_N, 0.4$  T)) for normal incidence is an order of magnitude larger than that for 45°-incidence excitation at 0 T ( $S(J_{\perp}, 0$  T)), indicating a Nernst effect that is much larger than the Seebeck effect as result of ambipolar transport and possibly anomalous Nernst effect, which will be discussed in the discussion section.

**THz emission from photo-Seebeck effect.** First, we study the characteristics of THz emission from Cd<sub>3</sub>As<sub>2</sub> without applying

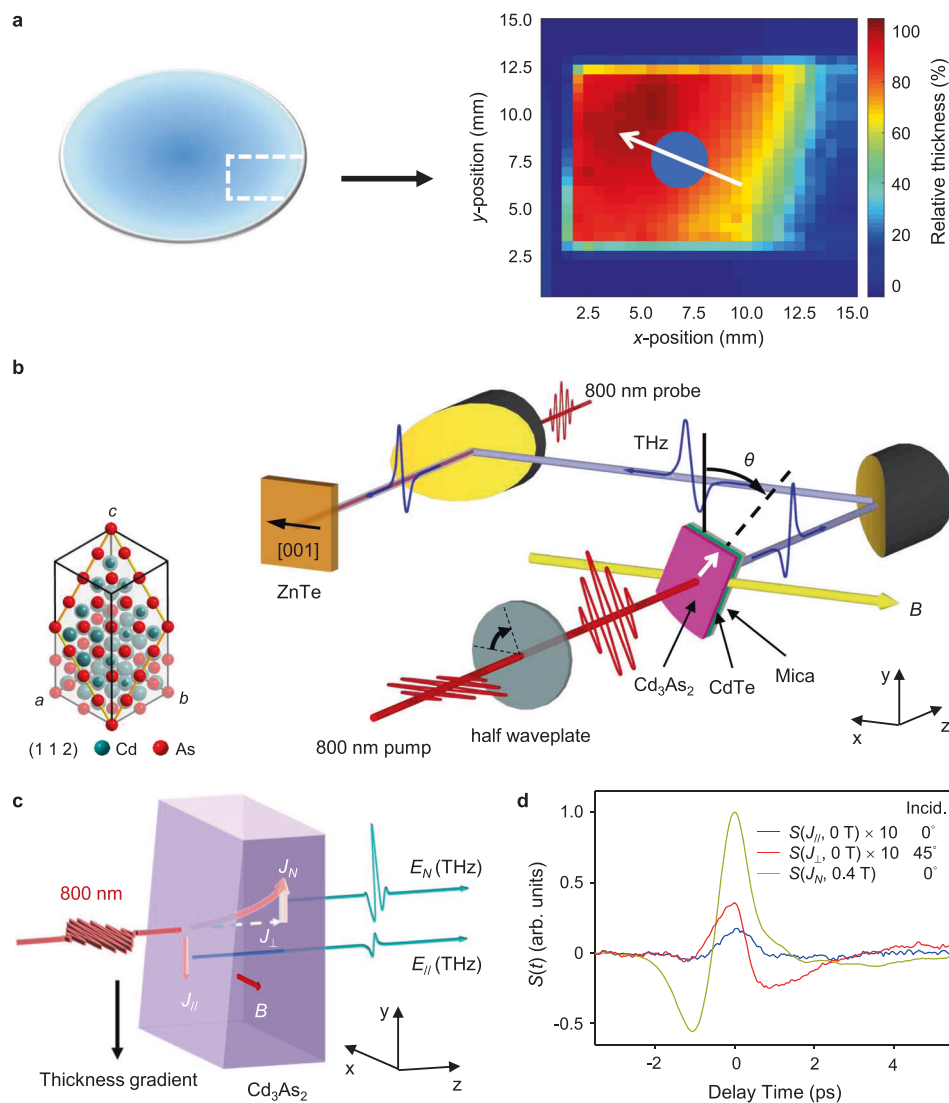


**Fig. 1 THz emissions from Cd<sub>3</sub>As<sub>2</sub> epitaxial film with a thickness gradient.** **a** The position of a cut piece (white dash line region) in an as-grown wafer, and the mapping of relative thickness of the Cd<sub>3</sub>As<sub>2</sub> film determined by two-dimensional scanning of laser transmittance. The blue circle marks the excitation laser spot and the arrow illustrates the direction of thickness gradient on the spot. **b** Schematic diagram of experimental setup, where  $\theta$  denotes the azimuthal angle of the sample with respect to  $y$ -axis. Inset: the crystal structure of Cd<sub>3</sub>As<sub>2</sub> along (112) plane. **c** Schematic diagram of THz emissions from transient current generated by 800-nm optical excitation.  $E_N$  and  $E_{//}$  here denote the instantaneous electrical field of THz emission from Nernst current ( $J_N$ ) under magnetic field and from the in-plane current ( $J_{//}$ ), respectively.  $J_{\perp}$  denotes the out-of-plane current. **d** Typical THz waveform generated by  $J_{//}$ ,  $J_{\perp}$  and  $J_N$  in **(c)**. The two THz waveforms from  $J_{\perp}$  and  $J_N$  are obtained by sample tilting and by applying an in-plane magnetic field respectively.

magnetic field. Figure 2a shows the peak amplitude of THz waveform ( $S_{\max}(t)$ , the waveforms are shown in Supplementary Fig. 4) increases with the excitation intensity ( $I$ ). It can be fitted by a model of photo-Seebeck current (see Supplementary Note 5), which approximately follows a power law:  $E_{\text{THz}} \propto I^{0.66}$ . This intensity dependence is different from that of an optical rectification effect or any other second-order effects<sup>17,32–41</sup>, which typically exhibits linear excitation intensity dependence. Here we can rule out the effect from absorption saturation of the excitation beam, because a power-dependent transmittance measurement of the 800-nm excitation beam is flat within the power range as shown in Supplementary Fig. 4a. Furthermore, the THz emission is independent of the polarization of the excitation beam as shown in Fig. 2b. This is consistent with the isotropic optical properties on Cd<sub>3</sub>As<sub>2</sub> (112) plane for near-infrared photon<sup>42–44</sup>. However, if the excitation polarization is fixed and the sample is rotated around the surface normal axis (varying the azimuthal angle  $\theta$ , as shown in the inset of Fig. 2c), the amplitude of the

THz waveform changes with  $\theta$  as shown in Fig. 2c. The peak signal of THz emission exhibits a cosinoidal dependence on  $\theta$  as shown in Fig. 2d. According to the cosinoidal fitting shown in Fig. 2d, we find the THz polarization direction is along the direction of thickness gradient of Cd<sub>3</sub>As<sub>2</sub> film with accuracy of 6.2°. This azimuthal angle dependence of THz emission is consistent with that the THz emission is generated via the in-plane Seebeck current  $J_{//}$  induced by thickness gradient<sup>16</sup> as discussed above.

**THz emission by photo-Nernst effect.** In the next, we study the characteristics of the THz emission measurement results when a 0.4-T in-plane magnetic field is applied. After applying the magnetic field along  $x$ -direction, the THz emission is about an order of magnitude larger. Figure 3a shows the excitation intensity dependence of THz emission amplitude in the presence of a magnetic field. Different from that at 0 T which follows the power law of  $E_{\text{THz}} \propto I^{0.66}$ , the excitation intensity dependence under

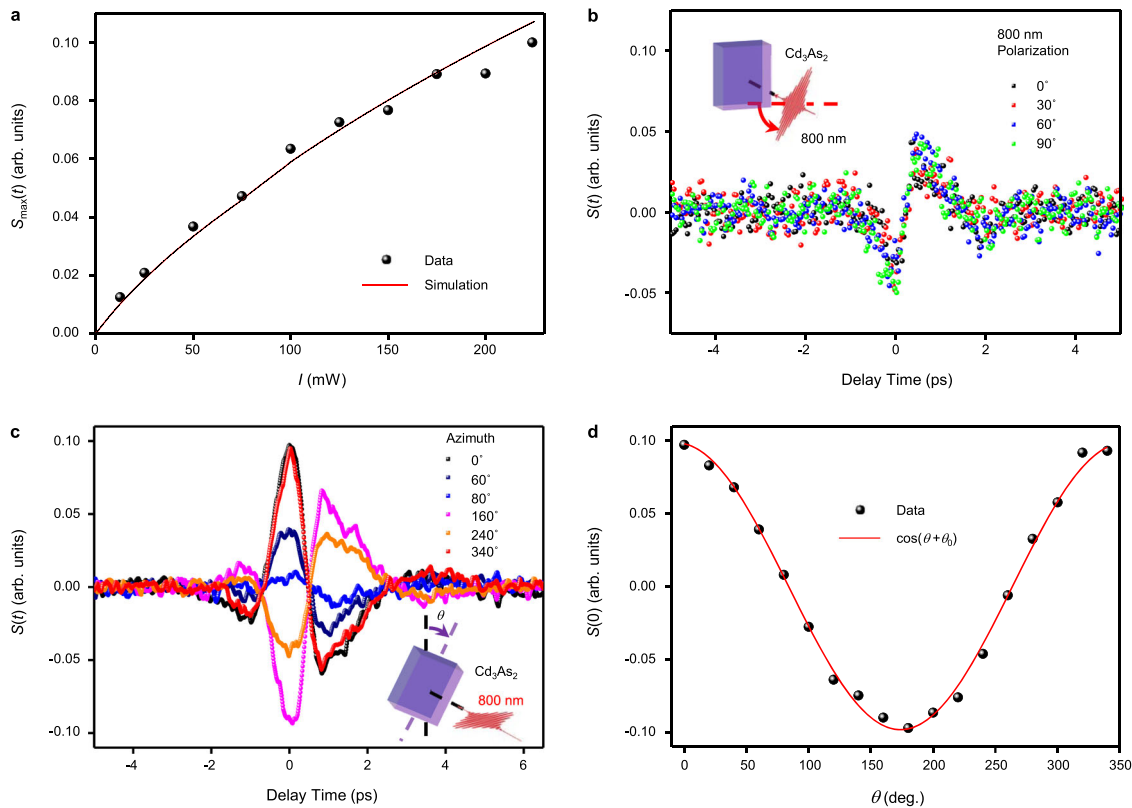


**Fig. 2 THz emission from  $\text{Cd}_3\text{As}_2$  without applying magnetic field.** **a** The laser intensity dependence of the peak field of emitted THz pulse. The red line is the simulation of power dependence according to the TE response presented in Supplementary Note 5. **b** Typical THz waveforms excited by laser with different polarized direction. **c** Typical THz waveforms at different azimuthal angle  $\theta$ , the thickness gradient is roughly set along  $y$ -axis for  $\theta = 0^\circ$ , with unintentional deviation of  $\theta_0$ . **d** The azimuthal angle dependence of the peak field of emitted THz pulse, and the red line is the cosinoidal fitting  $\cos(\theta + \theta_0)$ , the deviation ( $\theta_0$ ) is  $6.2^\circ$  according to the fitting. Insets in panels (**b**, **c**): the schematic illustrations of the corresponding measurements.

magnetic field follows a different power law of  $E_{\text{THz}} \propto I^{0.5}$ . The THz emission is also independent of the polarization of the excitation beam as shown in Fig. 3b. Both power and polarization dependence support the response is due to photothermal effect instead of nonlinear optical effect, which is similar to the case without magnetic field. Figure 3c shows the dependence of the THz waveforms at different azimuthal angle  $\theta$ . The THz response at 0.4 T magnetic field is composed of a  $\theta$ -dependent cosinoidal oscillation component and a  $\theta$ -independent component. The  $\theta$ -independent component is one order of magnitude larger than the  $\theta$ -dependent component. The  $\theta$ -dependent component is from  $J_{\parallel}$ , the oscillation amplitude of the  $\theta$ -dependent component is about the same for those taken with and without magnetic field as shown in Fig. 3d. The  $\theta$ -independent component is induced by the magnetic field due to photo-Nernst effect.

In the following, we systematically studied the magnetic field dependence of THz emission. First, we minimized the amplitude of nonmagnetic signal by adjusting  $\theta$ , therefore only the magnetic field-dependent THz component can be detected. We find the THz waveform can flip over and remain the same amplitude as the direction of the magnetic field is reversed as shown in Fig. 4a. However, if  $\theta$  is set so that there is a strong nonmagnetic signal, the directly detected THz signals are obviously asymmetric under reverse magnetic fields, unless the nonmagnetic component of the signal is subtracted (Supplementary Fig. 5). This further confirms that the THz emission under magnetic field contains a pure magnetic component ( $S(t, B) - S(t, 0)$ ) and a nonmagnetic component ( $S(t, 0)$ ) that are independent of each other, and the direction of magnetic component is affected by the direction of the magnetic field. Moreover, when the magnetic field is  $40^\circ$ -away

from the  $x$ -axis in  $xz$ -plane, the THz amplitude approximately equals to the THz amplitude under in-plane magnetic field multiplying by  $\cos 40^\circ$ , as show in Fig. 4b. It implies that only the in-plane projection of the magnetic field influences the detected THz emission.

The polarization of THz emission can be determined by measuring the orthogonal polarization THz components  $S_x$  and  $S_y$  along  $x$ - and  $y$ -axis, respectively (see the detailed method in Supplementary Note 3). As shown in Fig. 4c, for  $B \parallel x$ ,  $S_y$  dominates the signal and  $S_x$  is close to zero, so the THz emission is  $y$ -polarized; for  $B \parallel y$ , the magnetic THz becomes  $x$ -polarized. We can summarize that the polarization of THz emission is perpendicular to the in-plane magnetic field. The residual signal of  $S_x$  at  $B \parallel x$  and the THz amplitudes difference between  $B \parallel x$  and  $B \parallel y$  should be due to experimental errors, eg. ZnTe [001] or  $B$  not exactly along  $x/y$ -axis, and the inhomogeneity of ZnTe crystal. Practically, these errors are difficult to be removed completely. Finally, as shown in Fig. 4d, the pure magnetic THz component is linearly proportional to the in-plane magnetic field (THz waveforms presented in Supplementary Fig. 6).

## Discussion

The experimental evidences described above are consistent with the interpretations that the observed THz emission is dominated by transient PTE current. Due to the thickness gradient of the sample and strong absorption to the excitation light, the electron temperature gradient is generated after photoexcitation along both in-plane and out-of-plane directions which are responsible for detectable THz emission without and with magnetic field

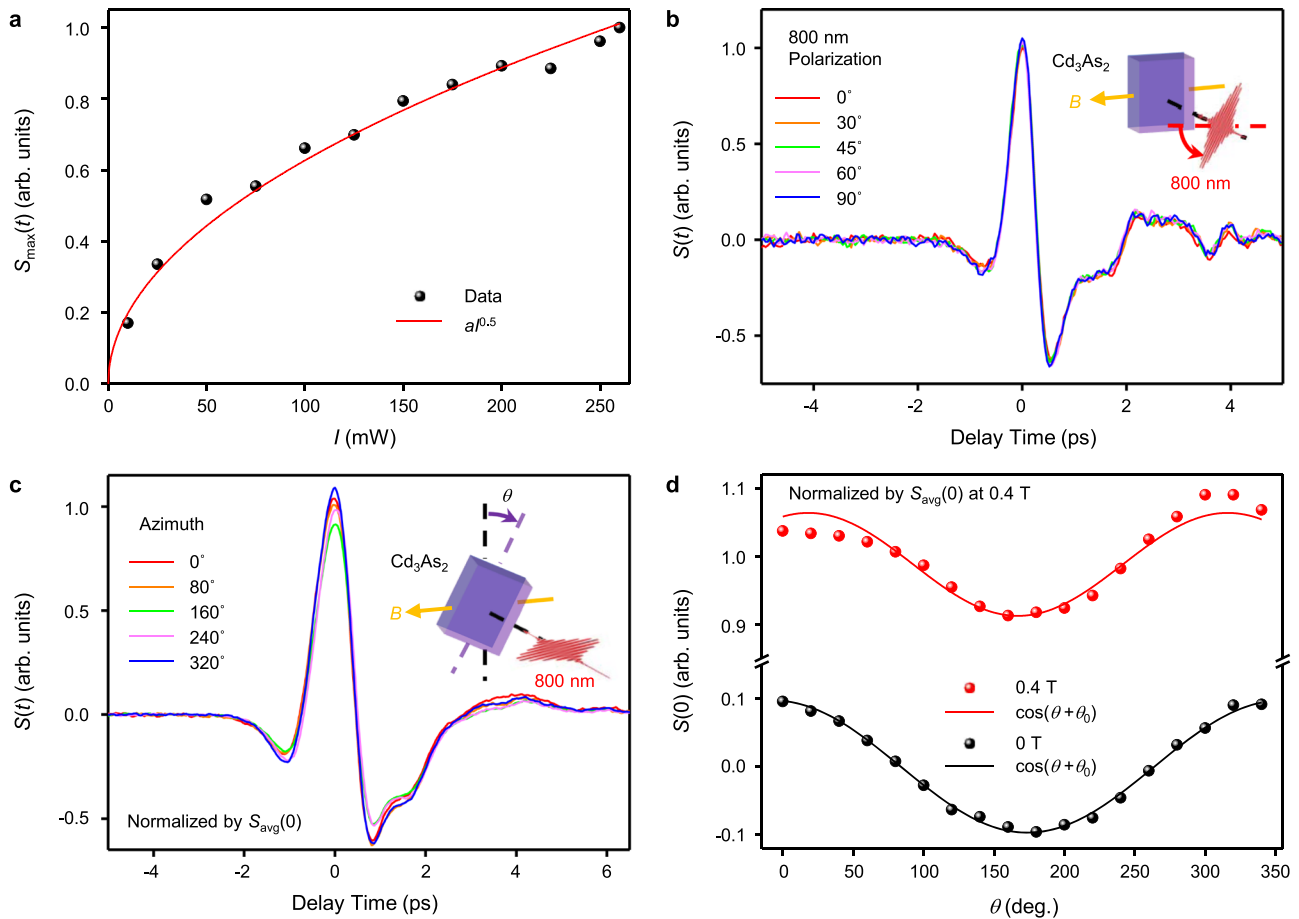


**Fig. 3 THz emission from Cd<sub>3</sub>As<sub>2</sub> with a magnetic field of -0.4 T at x-direction.** **a** The laser intensity dependence of the peak field of emitted THz pulse. The red line is a power-law fitting. **b** Typical THz waveforms excited by laser with different polarization. **c** Typical THz waveforms at different azimuthal angle  $\theta$ . **d** The azimuthal angle dependences of the peak field of THz pulses with and without magnetic field, and the lines are the cosinoidal fitting. The data are normalized by the average amplitude at time zero ( $S_{avg}(0)$ , 0.4 T). Insets in panels **(b, c)**: the schematic illustrations of the corresponding measurements.

respectively. According to the above experimental results, the THz emission polarized along  $y$ -axis, which is detectable in the E-O sampling configuration, can be given by the following empirical equation:

$$E_{THz} \propto I^{0.66} \hat{y} + bI^{0.5}(\hat{z} \times \mathbf{B}) \quad (1)$$

where  $b$  is a constant that corresponds to the ratio of Seebeck and Nernst contributions. The first term represents the contribution of THz emission generated from a transverse Seebeck effect due to thickness gradient that is independent of the magnetic field (as shown in Fig. 5a); the second term represents the contribution from the Nernst effect that is dependent on the magnetic field. These two terms exhibit different power-law dependences according to Figs. 2a and 3a, and the second term has a linear dependence on  $B$  according to Fig. 4d. The direction of the TE current is determined by the thermal gradient of the sample, which does not rely on the polarization of excitation light (as observed in Figs. 2b and 3b).

The sublinear excitation intensity dependence and the independence of the excitation polarization help to rule out other nonlinear optical effects which are usually considered as the mechanisms of THz emission. These effects include optical current injection, shift current, optical rectification, depletion field effect, photo-Dember effect and so on<sup>15,17,33–35,39,41</sup>. Although the second-order nonlinear tensor is zero due to the inversion symmetry of bulk Cd<sub>3</sub>As<sub>2</sub>, nonzero third-order tensor can exist

around an interface or by the assistance of a perpendicular DC electric field. However, those second-order nonlinear optical responses should have linear power dependence instead of sub-linear power dependence. The deduction of sublinear power dependence of the TE response, either the transverse Seebeck effect or the Nernst effect, is presented in Supplementary Note 5, by assuming that the intensity of transient currents is dominated by the laser-induced TE effects. The polarization independence is also consistent with the polarization-independent absorption of Cd<sub>3</sub>As<sub>2</sub>.

In the next, we analyze the TE response more quantitatively. The transient thermal electric current along  $y$ -axis ( $J_y(B)$ ), which emits THz emission that is detectable when setting [001] of ZnTe crystal along  $x$ -axis, is composed of two components:

$$J_y(B) = J_{S//}(B) + J_N(B) = \alpha_{yy}(B) \frac{dT_e}{dy} + \alpha_{yz}(B) \frac{dT_e}{dz} \quad (2)$$

where  $J_{S//}$  and  $J_N$  are the transverse Seebeck and the Nernst currents respectively,  $T_e$  is the instantaneous electron temperature, and  $\alpha_{yy}$ ,  $\alpha_{yz}$  are the TE conductivities of Seebeck and Nernst effect. When a magnetic field  $B$  is applied along  $x$  direction, the TE conductivities can be written as:  $\alpha_{yy} = \alpha_0 \frac{1}{1+(\mu B)^2}$  and  $\alpha_{yz} = \alpha_0 \frac{\mu B}{1+(\mu B)^2}$ , as derived from the linearized Boltzmann equation<sup>45</sup>, where  $\alpha_0$  is the zero-field TE conductivity and  $\mu$  is the carrier mobility. Taking  $\mu \sim 5000 \text{ cm}^2 \text{ V}^{-1} \text{ S}^{-1}$  according to our previous study<sup>28</sup>, and  $B \sim 0.4 \text{ T}$  in the



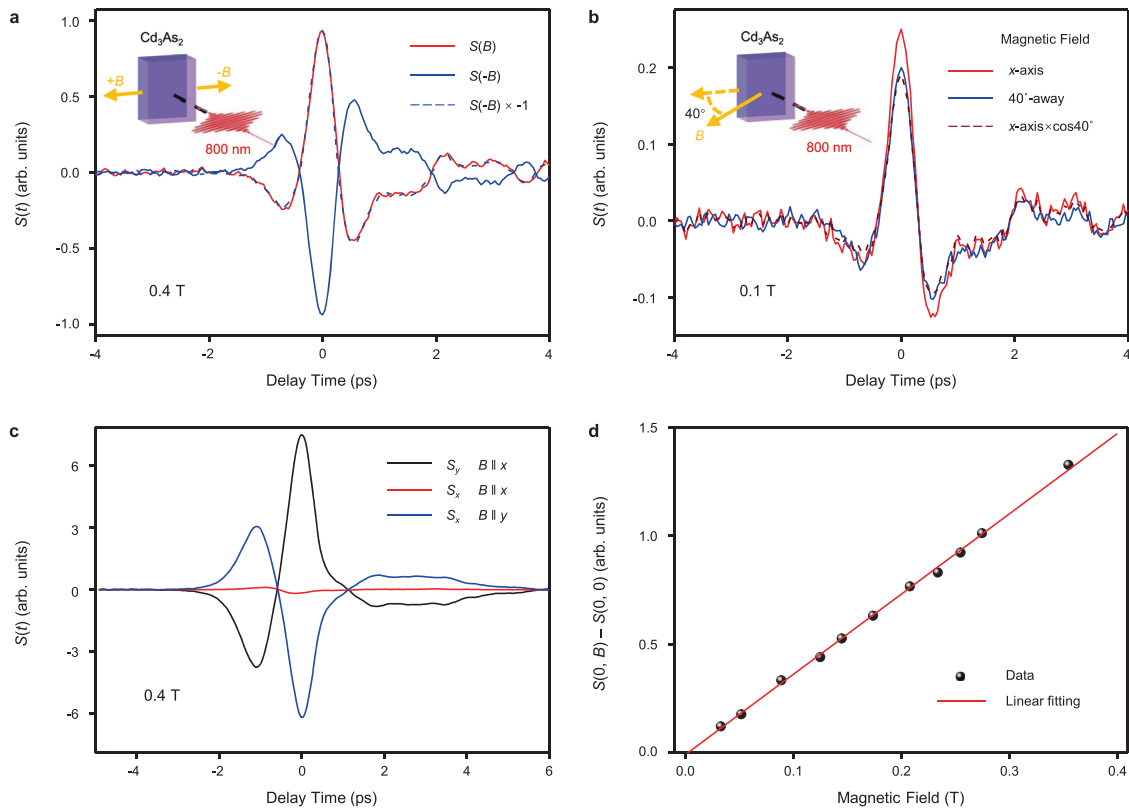


**Fig. 4** Magnetic field dependences of THz emission. **a** The THz emissions at reverse magnetic fields of 0.4 T. The dash line is the reversion of waveform at  $B = -0.4$  T. **b** The THz emissions when a 0.1 T-magnetic field is applied at  $x$ -axis and  $40^\circ$  away from  $x$ -axis in  $xz$ -plane, respectively. The dash line is the THz waveform under  $x$ -directional magnetic field multiplying by  $\cos 40^\circ$ . **c** The  $x$ - and  $y$ -polarization components of the THz emissions with magnetic field  $B \parallel x$  and  $B \parallel y$ . **d** The amplitude of net magnetic THz signal at time zero as a function of the intensity of magnetic field. Insets in panels (**a**, **b**): the schematic illustrations of the corresponding measurements.

measurement,  $(\mu B)^2 \sim 0.04 \ll 1$ . Therefore,

$$J_y(B) \approx \alpha_0 \frac{dT_e}{dy} + \mu B \alpha_0 \frac{dT_e}{dz} \quad (3)$$

which is fully consistent with empirical Eq. 1 summarized from the experimental observation. According to Eq. 3, the second term (Nernst current  $J_N$ ) should be smaller than the longitudinal Seebeck current  $J_{S\perp} = \alpha_0 \frac{dT_e}{dz}$ , this is inconsistent with the experimental observation that  $J_N$  is over an order of magnitude larger than  $J_{S\perp}$  as shown in Fig. 1d and Supplementary Fig. 2d.

This large Nernst signal is due to the ambipolar transport nature during the transient process as illustrated in Fig. 5b. To describe the Nernst response, Eq. 3 would become  $J_y(B) \approx \alpha_{e0} \frac{dT_e}{dy} - \alpha_{h0} \frac{dT_h}{dy} + \mu_e B \alpha_{e0} \frac{dT_e}{dz} + \mu_h B \alpha_{h0} \frac{dT_h}{dz}$ , where  $e$  and  $h$  denote the electron and hole respectively. In the right side of this equation, the first two terms are contributions from electron and hole to  $J_{S\parallel}$  respectively, and the last two terms are contributions to  $J_N$ . These two types of carriers have the same longitudinal thermal diffusion direction, counterbalancing each other's contribution to the Seebeck current. However, distinct from the Seebeck effect, the electrons and holes are deflected in opposite directions under magnetic field, and thus, their contributions to the Nernst current are added together as shown in Fig. 5b. The lifetime scale of photoexcited electrons and holes are consistent with recent experimental observation that the photoexcited electrons and holes have an approximate lifetime of 3 ps before recombination in a Tr-ARPES measurement<sup>46</sup>. The picosecond photoexcited carrier lifetime is sufficient to support the transient ambipolar transport on picosecond timescale and the

subsequently enhanced THz emission. Usually, it is not easy to observe the ambipolar transport in low-temperature electrical transport measurement, because one type of carriers predominated in heavily doped semimetals. Previously, the Nernst signal enhancement had been observed in compensated semimetals such as bismuth and graphite hosting almost equal concentrations of electrons and holes under transport measurement without photoexcitation<sup>45,47,48</sup>. The transient PTE response and suitable photoexcited carrier lifetime of  $\text{Cd}_3\text{As}_2$  provide an ideal experimental platform to observe the enhancement on Nernst effect as demonstrated in this work.

Additionally, the anomalous Nernst effect may also contribute to the large enhancement of the PTE signal under magnetic field<sup>49,50</sup>. The anomalous Nernst effect arises from the nonzero Berry curvature associated with the Weyl nodes without the need to apply a real magnetic field. However, it should be absent in Dirac semimetal without applying magnetic field due to restoration of time-reversal symmetry. When a magnetic field is applied, the magnetic field can split a Dirac node into a pair of Weyl nodes with opposite chirality, and then a nonzero Berry curvature is generated. It has been found that the Berry curvature can induce an anomalous Nernst effect to add on the conventional one<sup>6,49-51</sup>. At low magnetic field and low temperature, it is predicted theoretically that the total Nernst effect is characterized by an almost steplike profile at the low magnetic field and the response is dominated by the anomalous Nernst effect<sup>49,50</sup>. Although in this work, we cannot clearly sort out the contribution from conventional and anomalous Nernst effects, the large enhancement factor implies very possible contribution from anomalous Nernst response, which calls for further studies.

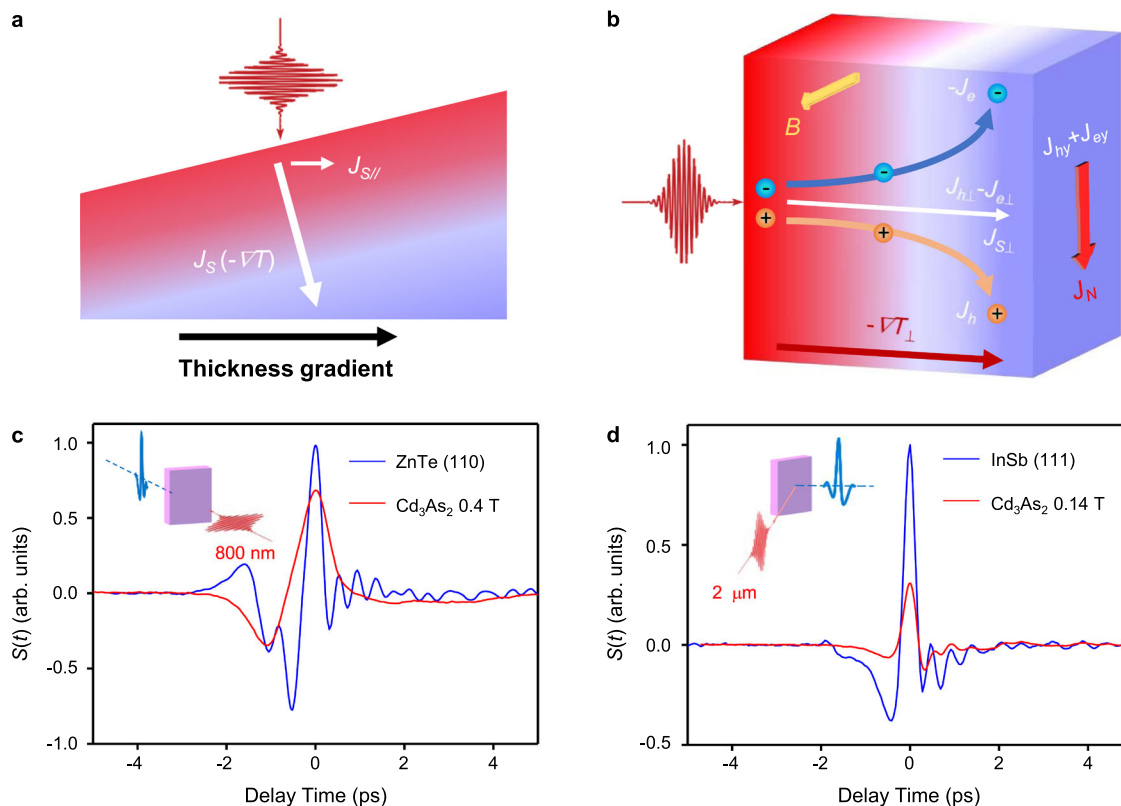


**Fig. 5 Mechanisms of PTE THz emissions and the comparison with semiconductor THz sources.** Schematics of (a) transverse Seebeck effect and (b) Nernst effect, where  $J_S$  is the Seebeck current,  $J_{S//}$  is the in-plane component,  $J_{S\perp}$  and  $J_N$  denote the out-of-plane component and the Nernst current respectively, which are composed by both the electron current and hole current. Comparison of the optimized THz emission from  $\text{Cd}_3\text{As}_2$  nano-films with the (c) ZnTe (110) and (d) InSb (111) wafers with thicknesses of 0.5 mm, respectively. Insets in panels (c, d): the corresponding setups.

At last, we compared the THz emission from  $\text{Cd}_3\text{As}_2$  by photo-Nernst effect at the weak magnetic field with that from the typical semiconductor THz sources. Figure 5c compares the THz intensity from the response with ZnTe, which is the most widely used THz crystal through optical rectification<sup>52</sup>. The intensity of THz emission from  $\text{Cd}_3\text{As}_2$  at 0.4 T can reach ~70% of that from 0.5 mm-thick ZnTe optimized under the same excitation condition. Figure 5d further compare the THz emission from  $\text{Cd}_3\text{As}_2$  with that from a 0.5 mm-thick InSb (111), which is one of the best narrow bandgap semiconductors for THz source with the dominated mechanism of photo-Dember effect<sup>34,35,53</sup>. The intensity of THz emission from  $\text{Cd}_3\text{As}_2$  at 0.14 T can reach ~30% of that from InSb under a reflective detection geometry with 2- $\mu\text{m}$  excitation, confirming the thermoelectric THz emission can also be triggered by longer wavelength due to the zero-bandgap nature of  $\text{Cd}_3\text{As}_2$ . The comparison measurements indicate that, based on the photoexcited transient Nernst effect, the THz emission efficiency from  $\text{Cd}_3\text{As}_2$  with the thickness of tens nanometer is already comparable with typical semiconductor THz sources with submillimeter thickness. When integrated with ferromagnetic materials with careful design<sup>54–58</sup>, it would provide a highly efficient compact THz source solution based on photo-Nernst effect.

In summary, we have studied THz emissions generated from transient PTE current in  $\text{Cd}_3\text{As}_2$  by femtosecond laser excitation under zero and weak magnetic field at room temperature. The THz emissions are generated from a thickness-gradient-assisted transverse Seebeck and Nernst effect, respectively. The magnitude of photo-Nernst current is an order of magnitude larger than Seebeck current at low magnetic field indicating ambipolar

transport nature after the photoexcitation. Because of the Nernst effect, THz emission efficiency is comparable to ZnTe and InSb crystals. The THz emission of  $\text{Cd}_3\text{As}_2$  can be triggered by ultrafast laser with wavelength over broad-spectrum range due to its semimetallic nature. In addition, the THz emission can be versatility controlled through optical, electric, magnetic and thermal approaches. Compared with its two-dimensional Dirac semimetal counterpart, graphene, which has shown strong and fast PTE responses<sup>10,25,59</sup>,  $\text{Cd}_3\text{As}_2$  has larger steady-state TE coefficients and smaller thermal conductivity<sup>49,60–64</sup>, which are both more favorable for TE conversion than graphene and thus promises better PTE response at transient state. We expect the transient PTE dynamics revealed in this work provides indispensable device physics for high speed/field electronic and optoelectronic device applications based on three-dimensional topological semimetals.

## Methods

**Sample preparation.**  $\text{Cd}_3\text{As}_2$  thin films with about 50-nm thickness were grown in a PerkinElmer (Waltham, MA) 425B molecular beam epitaxy system. Fresh cleaved 2-inch mica was used as the substrate. The data presented in the main text are obtained from two samples with substrate thickness of 30  $\mu\text{m}$  and 70  $\mu\text{m}$ , respectively. The adsorbed molecules on the surface of the substrate were removed by annealing at 300 °C for 30 min. Then a CdTe buffer layer with a thickness of approximately 10 nm was deposited on the substrate to assist  $\text{Cd}_3\text{As}_2$  nucleation. After that, the  $\text{Cd}_3\text{As}_2$  layer was grown on the buffer layer by evaporating the bulk material (99.9999%, American Elements Inc., Los Angeles, CA) at 170 °C. The growth was in situ monitored by the reflection high-energy electron diffraction system. The  $\text{Cd}_3\text{As}_2$  layer has high quality and excellent electric properties, which have been systematically studied in previous works<sup>28–30</sup>. The relative thickness mapping of  $\text{Cd}_3\text{As}_2$  film is determined by two-dimensional transmittance scanning with a 633-nm cw laser. The laser spot size is about 1 mm, and the scanning step is 0.5 mm.

**Transient THz emission setup.** In a default experimental configuration, 150-fs laser pulses with a central wavelength of 800 nm from a 250-kHz Ti-sapphire amplifier (RegA) system<sup>65</sup> were used to excite the samples and to probe the emitted THz pulses through a 0.5 mm-thick ZnTe (110) crystal using a standard E-O sampling technique<sup>66</sup>. The excitation beam propagates along the  $z$ -direction. It passes through a 3-mm-diameter aperture to shape a circular excitation beam, and the full width at half maximum is about 1.6 mm. The excitation power is measured just in front of the sample and chopped with a frequency about 1 kHz. A half waveplate is mounted into the setup to adjust the polarization direction of the excitation beam before incident onto a sample. The incident angle could be adjusted by tilting the sample in  $xz$ -plane, and it is defined as  $0^\circ$  for normal incidence on the Cd<sub>3</sub>As<sub>2</sub> side. The THz pulse was emitted along the  $z$ -direction, and then it was collected and focused onto the ZnTe crystal using a pair of parabolic mirrors, which is collimated with a  $y$ -polarized sampling beam. Because the E-O sampling is THz polarization dependent<sup>67</sup>, in general measurements, the ZnTe [001] axis is set along  $x$ -direction to detect  $y$ -polarized THz component. To acquire the  $x$ -component, ZnTe [001] axis could be set along  $y$ -directions. In magneto measurements, a pair of permanent magnets was applied along  $x$ -direction. The intensity of the magnetic field could be controlled by change the spacing between the two magnets. The maximum magnetic field can reach 0.4 T in this setup. In out-of-plane magnetic field measurement, the magnetic field is applied with an approximately  $40^\circ$ -angle with respect to the  $x$ -axis in  $xz$ -plane, and the intensity is lowered to 0.1 T to get a larger space between the permanent magnets to permit the unhindered passing through of the THz wave. In comparative measurement with InAs (111), a reflective setup was used and the excitation beam with a wavelength of 2  $\mu$ m was from an optical parametric amplification. The light is incidence on the  $45^\circ$ -tilted sample along  $x$ -direction. the magnetic field can only reach 0.14 T and the direction of the magnetic field has to set along  $y$ -direction as limited by the reflection geometry. All measurements were carried out in atmosphere condition at room temperature.

## Data availability

The source data underlying Fig. 1a, d, 2, 3, 4, and 5c, d are provided as a Source Data file [<https://doi.org/10.6084/m9.figshare.18482018>]. Other data is available from the corresponding author upon reasonable request.

Received: 1 October 2021; Accepted: 17 February 2022;

Published online: 25 March 2022

## References

- Goldsmid, H. J. *Introduction to Thermoelectricity* (Springer, 2010).
- Xiang, J. et al. Anisotropic thermal and electrical transport of Weyl semimetal TaAs. *J. Phys.: Condens. Matter* **29**, 485501 (2017).
- Cagliaris, F. et al. Anomalous Nernst effect and field-induced Lifshitz transition in the Weyl semimetals TaP and TaAs. *Phys. Rev. B* **98**, 201107 (2018).
- Fu, C. et al. Large Nernst power factor over a broad temperature range in polycrystalline Weyl semimetal NbP. *Energy Environ. Sci.* **11**, 2813–2820 (2018).
- Rana, K. G. et al. Thermopower and Unconventional Nernst Effect in the Predicted Type-II Weyl Semimetal WTe<sub>2</sub>. *Nano Lett.* **18**, 6591–6596 (2018).
- Fu, C., Sun, Y. & Felser, C. Topological thermoelectrics. *APL Mater.* **8**, 040913 (2020).
- Han, F. et al. Quantized thermoelectric Hall effect induces giant power factor in a topological semimetal. *Nat. Commun.* **11**, 6167 (2020).
- Xia, F., Wang, H., Xiao, D., Dubey, M. & Ramasubramanian, A. Two-dimensional material nanophotonics. *Nat. Photonics* **8**, 899–907 (2014).
- Sun, D. et al. Ultrafast Relaxation of Excited Dirac Fermions in Epitaxial Graphene Using Optical Differential Transmission Spectroscopy. *Phys. Rev. Lett.* **101**, 157402 (2008).
- Sun, D. et al. Ultrafast hot-carrier-dominated photocurrent in graphene. *Nat. Nanotechnol.* **7**, 114–118 (2012).
- Wang, Q. et al. Ultrafast Broadband Photodetectors Based on Three-Dimensional Dirac Semimetal Cd<sub>3</sub>As<sub>2</sub>. *Nano Lett.* **17**, 834–841 (2017).
- Zhu, C. et al. A robust and tuneable mid-infrared optical switch enabled by bulk Dirac fermions. *Nat. Commun.* **8**, 14111 (2017).
- Lu, W. et al. Ultrafast relaxation dynamics of photoexcited Dirac fermions in the three-dimensional Dirac semimetal Cd<sub>3</sub>As<sub>2</sub>. *Phys. Rev. B* **95**, 024303 (2017).
- Zhuo, X. et al. Dynamical evolution of anisotropic response of type-II Weyl semimetal TaIrTe<sub>4</sub> under ultrafast photoexcitation. *Light.: Sci. Appl.* **10**, 101 (2021).
- Laman, N., Bieler, M. & Driel, H. M. V. Ultrafast shift and injection currents observed in wurtzite semiconductors via emitted terahertz radiation. *J. Appl. Phys.* **98**, 103507 (2005).
- Takahashi, K. et al. Terahertz Radiation via Ultrafast Manipulation of Thermoelectric Conversion in Thermoelectric Thin Films. *Adv. Optical Mater.* **2**, 428–434 (2014).
- Braun, L. et al. Ultrafast photocurrents at the surface of the three-dimensional topological insulator Bi<sub>2</sub>Se<sub>3</sub>. *Nat. Commun.* **7**, 13259 (2016).
- Liang, T. et al. Ultrahigh mobility and giant magnetoresistance in the Dirac semimetal Cd<sub>3</sub>As<sub>2</sub>. *Nat. Mater.* **14**, 280–284 (2015).
- Liu, J., Xia, F., Xiao, D., García de Abajo, F. J. & Sun, D. Semimetals for high-performance photodetection. *Nat. Mater.* **19**, 830–837 (2020).
- Sha, W., Rhee, J., Norris, T. B. & Schaff, W. J. Transient carrier and field dynamics in quantum-well parallel transport: From the ballistic to the quasi-equilibrium regime. *IEEE J. Quantum Electron.* **28**, 2445–2455 (1992).
- Leitenstorfer, A., Hunsche, S., Shah, J., Nuss, M. C. & Knox, W. H. Femtosecond Charge Transport in Polar Semiconductors. *Phys. Rev. Lett.* **82**, 5140–5143 (1999).
- Brodtschelm, A., Schöllhorn, C., Kasper, E. & Leitenstorfer, A. Ultrafast high-field transport after 10 fs hot carrier injection in Si and SiGe. *Semiconductor Sci. Technol.* **19**, S267–S269 (2004).
- Dai, C.-H. et al. Hot carrier effect on gate-induced drain leakage current in high-k/metal gate n-channel metal-oxide-semiconductor field-effect transistors. *Appl. Phys. Lett.* **99**, 012106 (2011).
- Ge, S. et al. Dynamical Evolution of Anisotropic Response in Black Phosphorus under Ultrafast Photoexcitation. *Nano Lett.* **15**, 4650–4656 (2015).
- Gabor Nathaniel, M. et al. Hot Carrier-Assisted Intrinsic Photoresponse in Graphene. *Science* **334**, 648–652 (2011).
- Lai, J. et al. Anisotropic Broadband Photoresponse of Layered Type-II Weyl Semimetal MoTe<sub>2</sub>. *Adv. Mater.* **30**, 1707152 (2018).
- Ma, J. et al. Experimental progress on layered topological semimetals. *2D Mater.* **6**, 032001 (2019).
- Lu, W., Ling, J., Xiu, F. & Sun, D. Terahertz probe of photoexcited carrier dynamics in the Dirac semimetal Cd<sub>3</sub>As<sub>2</sub>. *Phys. Rev. B* **98**, 104310 (2018).
- Liu, Y. et al. Gate-tunable quantum oscillations in ambipolar Cd<sub>3</sub>As<sub>2</sub> thin films. *NPG Asia Mater.* **7**, e221–e221 (2015).
- Cheng, P. et al. Thickness-dependent quantum oscillations in Cd<sub>3</sub>As<sub>2</sub> thin films. *N. J. Phys.* **18**, 083003 (2016).
- Lu, W. et al. Coherent diffraction rings induced by thermal-mechanical effect of a flexible Dirac semimetallic composite structure. *J. Appl. Phys.* **129**, 093102 (2021).
- Hilton, D. J. et al. Terahertz emission via ultrashort-pulse excitation of magnetic metal films. *Opt. Lett.* **29**, 1805–1807 (2004).
- Kadlec, F., Kužel, P. & Coutaz, J.-L. Optical rectification at metal surfaces. *Opt. Lett.* **29**, 2674–2676 (2004).
- Gu, P. & Tani, M. Terahertz Radiation from Semiconductor Surfaces. In: *Terahertz Optoelectronics*. (Springer Berlin Heidelberg, 2005).
- Malevich, V. L., Adomavicius, R. & Krotkus, A. THz emission from semiconductor surfaces. *Comptes Rendus Phys.* **9**, 130–141 (2008).
- Ahn, H., Yeh, Y. J., Hong, Y. L. & Gwo, S. Terahertz emission mechanism of magnesium doped indium nitride. *Appl. Phys. Lett.* **95**, 232104 (2009).
- Ramakrishnan, G. & Planken, P. C. M. Percolation-enhanced generation of terahertz pulses by optical rectification on ultrathin gold films. *Opt. Lett.* **36**, 2572–2574 (2011).
- Kajikawa, K. et al. Terahertz emission from surface-immobilized gold nanospheres. *Opt. Lett.* **37**, 4053–4055 (2012).
- Maysonave, J. et al. Terahertz Generation by Dynamical Photon Drag Effect in Graphene Excited by Femtosecond Optical Pulses. *Nano Lett.* **14**, 5797–5802 (2014).
- Hamh, S. Y. et al. Helicity-dependent photocurrent in a Bi<sub>2</sub>Se<sub>3</sub> thin film probed by terahertz emission spectroscopy. *Phys. Rev. B* **94**, 161405 (2016).
- Guzelturk, B. et al. Terahertz Emission from Hybrid Perovskites Driven by Ultrafast Charge Separation and Strong Electron-Phonon Coupling. *Adv. Mater.* **30**, 1704737 (2018).
- Akrap, A. et al. Magneto-Optical Signature of Massless Kane Electrons in Cd<sub>3</sub>As<sub>2</sub>. *Phys. Rev. Lett.* **117**, 136401 (2016).
- Mosca Conte, A., Pulci, O. & Bechstedt, F. Electronic and optical properties of topological semimetal Cd<sub>3</sub>As<sub>2</sub>. *Sci. Rep.* **7**, 45500 (2017).
- Hakl, M. et al. Energy scale of Dirac electrons in Cd<sub>3</sub>As<sub>2</sub>. *Phys. Rev. B* **97**, 115206 (2018).
- Behnia, K. *Fundamentals of Thermoelectricity* (Oxford Scholarship Online, 2015).
- Bao, C. et al. Population inversion and Dirac fermion cooling in 3D Dirac semimetal Cd<sub>3</sub>As<sub>2</sub>. *Nano Letters* **22**, 1138–1144 <https://doi.org/10.1021/acs.nanolett.1c04250> (2022).
- Behnia, K., Méasson, M.-A. & Kopelevich, Y. Oscillating Nernst-Edtinghausen Effect in Bismuth across the Quantum Limit. *Phys. Rev. Lett.* **98**, 166602 (2007).
- Zhu, Z., Yang, H., Fauqué, B., Kopelevich, Y. & Behnia, K. Nernst effect and dimensionality in the quantum limit. *Nat. Phys.* **6**, 26–29 (2010).



49. Liang, T. et al. Anomalous Nernst Effect in the Dirac Semimetal  $\text{Cd}_3\text{As}_2$ . *Phys. Rev. Lett.* **118**, 136601 (2017).
50. Sharma, G., Moore, C., Saha, S. & Tewari, S. Nernst effect in Dirac and inversion-asymmetric Weyl semimetals. *Phys. Rev. B* **96**, 195119 (2017).
51. Wang, P. et al. Giant Nernst effect and field-enhanced transversal zNT in  $\text{ZrTe}_5$ . *Phys. Rev. B* **103**, 045203 (2021).
52. Nahata, A., Weling, A. S. & Heinz, T. F. A wideband coherent terahertz spectroscopy system using optical rectification and electro-optic sampling. *Appl. Phys. Lett.* **69**, 2321–2323 (1996).
53. Gu, P., Tani, M., Kono, S., Sakai, K. & Zhang, X. C. Study of terahertz radiation from InAs and InSb. *J. Appl. Phys.* **91**, 5533–5537 (2002).
54. Seifert, T. et al. Efficient metallic spintronic emitters of ultrabroadband terahertz radiation. *Nat. Photonics* **10**, 483–488 (2016).
55. Wang, Z., Tang, C., Sachs, R., Barlas, Y. & Shi, J. Proximity-Induced Ferromagnetism in Graphene Revealed by the Anomalous Hall Effect. *Phys. Rev. Lett.* **114**, 016603 (2015).
56. Katmis, F. et al. A high-temperature ferromagnetic topological insulating phase by proximity coupling. *Nature* **533**, 513–516 (2016).
57. Tang, C. et al. Above 400-K robust perpendicular ferromagnetic phase in a topological insulator. *Sci. Adv.* **3**, e1700307 (2017).
58. Ng, S. M. et al. High-Temperature Anomalous Hall Effect in a Transition Metal Dichalcogenide Ferromagnetic Insulator Heterostructure. *ACS Nano* **14**, 7077–7084 (2020).
59. Cao, H. et al. Photo-Nernst current in graphene. *Nat. Phys.* **12**, 236–239 (2016).
60. Jia, Z. et al. Thermoelectric signature of the chiral anomaly in  $\text{Cd}_3\text{As}_2$ . *Nat. Commun.* **7**, 13013 (2016).
61. Wang, H. et al. Magnetic Field-Enhanced Thermoelectric Performance in Dirac Semimetal  $\text{Cd}_3\text{As}_2$  Crystals with Different Carrier Concentrations. *Adv. Funct. Mater.* **29**, 1902437 (2019).
62. Wei, P., Bao, W., Pu, Y., Lau, C. N. & Shi, J. Anomalous Thermoelectric Transport of Dirac Particles in Graphene. *Phys. Rev. Lett.* **102**, 166808 (2009).
63. Seol, J. et al. Two-Dimensional Phonon Transport in Supported Graphene. *Science* **328**, 213–216 (2010).
64. Balandin, A. A. et al. Superior Thermal Conductivity of Single-Layer Graphene. *Nano Lett.* **8**, 902–907 (2008).
65. Norris, T. B. Femtosecond pulse amplification at 250 kHz with a Ti:sapphire regenerative amplifier and application to continuum generation. *Opt. Lett.* **17**, 1009–1011 (1992).
66. Gallot, G. & Grischkowsky, D. Electro-optic detection of terahertz radiation. *J. Opt. Soc. Am. B* **16**, 1204–1212 (1999).
67. Planken, P. C. M., Nienhuys, H.-K., Bakker, H. J. & Wenckebach, T. Measurement and calculation of the orientation dependence of terahertz pulse detection in ZnTe. *J. Opt. Soc. Am. B* **18**, 313–317 (2001).

## Acknowledgements

This project has been supported by the National Key Research and Development Program of China (Grant No. 2020YFA0308800, 2021YFA1400100), the National Natural Science Foundation of China (Grant No. 12034001). D.S. acknowledges Beijing Nature

Science Foundation (Grant No. JQ19001). F.X. acknowledges the supports from the Science and Technology Commission of Shanghai (Grant No. 19511120500), the Shanghai Municipal Science and Technology Major Project (Grant No. 2019SHZDZX01) and the Program of Shanghai Academic/Technology Research Leader (Grant No. 20XD1400200). J.C. acknowledges support from the Scientific Research Project of the Chinese Academy of Sciences (Grant No. QYZDB-SSW-SYS038). J.Lai is also supported by China Postdoctoral Science Foundation (Grant No. 2021M690231) and China National Postdoctoral Program for Innovative Talent (Grant No. BX20200015).

## Author contributions

D.S. and W.L. conceived the project. L.W., Z.F., J.M., J.Lai, X.S., X.Z., and Z.X. performed the optical experiments under the supervision of D.S. Y.Y. prepared the  $\text{Cd}_3\text{As}_2$  samples and performed the basic characterizations under the supervision of F.X. J.C., S.Z., J.Liu, and X.H. contributed to the results analysis. W.L. and D.S. wrote the paper, assisted by Z.F., J.M., X.Z., and Z.X. All the authors commented on the paper.

## Competing interests

The authors declare no competing interests.

## Additional information

**Supplementary information** The online version contains supplementary material available at <https://doi.org/10.1038/s41467-022-29168-w>.

**Correspondence** and requests for materials should be addressed to Dong Sun.

**Peer review information** *Nature Communications* thanks Su-Yang Xu and the other anonymous reviewers for their contribution to the peer review of this work.

**Reprints and permission information** is available at <http://www.nature.com/reprints>

**Publisher's note** Springer Nature remains neutral with regard to jurisdictional claims in published maps and institutional affiliations.



**Open Access** This article is licensed under a Creative Commons Attribution 4.0 International License, which permits use, sharing, adaptation, distribution and reproduction in any medium or format, as long as you give appropriate credit to the original author(s) and the source, provide a link to the Creative Commons license, and indicate if changes were made. The images or other third party material in this article are included in the article's Creative Commons license, unless indicated otherwise in a credit line to the material. If material is not included in the article's Creative Commons license and your intended use is not permitted by statutory regulation or exceeds the permitted use, you will need to obtain permission directly from the copyright holder. To view a copy of this license, visit <http://creativecommons.org/licenses/by/4.0/>.

© The Author(s) 2022